Title
An accelerated photo-magnetic imaging reconstruction algorithm based on an analytical forward solution and a fast Jacobian assembly method

Journal
Physics in Medicine and Biology, 61(20)

ISSN
0031-9155

Authors
Nouizi, F
Erkol, H
Luk, A
et al.

Publication Date
2016-10-21

DOI
10.1088/0031-9155/61/20/7448

Peer reviewed

HHS Public Access

Author manuscript

Phys Med Biol. Author manuscript; available in PMC 2018 April 03.

Published in final edited form as:

Phys Med Biol. 2016 October 21; 61(20): 7448–7465. doi:10.1088/0031-9155/61/20/7448.

An accelerated Photo-Magnetic Imaging reconstruction algorithm based on an analytical forward solution and a fast Jacobian assembly method

F Nouizi[1], **H Erkol**[1,3], **A Luk**[1], **M Marks**[2], **MB Unlu**[3], and **G Gulsen**[1,2]

[1]Tu and Yuen Center for Functional Onco-Imaging, Department of Radiological Sciences, University of California, Irvine, CA, USA

[2]Department of Biomedical Engineering, University of California, Irvine, CA, USA

[3]Department of Physics, Bogazici University, Bebek, Istanbul, Turkey

Abstract

We previously introduced Photo-Magnetic Imaging (PMI), an imaging technique that illuminates the medium under investigation with near-infrared light and measures the induced temperature increase using Magnetic Resonance Thermometry (MRT). Using a multiphysics solver combining photon migration and heat diffusion, PMI models the spatiotemporal distribution of temperature variation and recovers high resolution optical absorption images using these temperature maps. In this paper, we present a new fast non iterative reconstruction algorithm for PMI. This new algorithm uses analytic methods during the resolution of the forward problem and the assembly of the sensitivity matrix. We validate our new analytic-based algorithm with the first generation Finite Element Method (FEM) based reconstruction algorithm previously developed by our team. The validation is performed using, first synthetic data and afterwards, real MRT measured temperature maps. Our new method accelerates the reconstruction process 30-fold when compared to a single iteration of the FEM-based algorithm.

Keywords

photon propagation; diffuse optical tomography; photo-magnetic imaging

1. Introduction

Diffuse optical tomography (DOT) is an optical imaging technique principally used to recover the spatial distribution of optical absorption and scattering of biological tissue [1–9]. This technique is able to probe several centimeters deep tissues owing to low tissue absorption in the near-infrared (NIR) spectral window [10]. This advantage makes DOT a suitable functional imaging technique for a variety of applications ranging from breast [11–13] and brain functional imaging [14–17] to small animals imaging [18–20].

Despite its high sensitivity, DOT is characterized with a very poor spatial resolution. This is principally caused by high tissue scattering affecting the pathlength of the photons propagating inside the tissue. In addition, DOT image reconstruction is based on the resolution of a highly ill-posed inverse problem yielding to non-unique solutions [21].

Basically, this arises from the DOT measurement acquisition scheme where the light sources and detectors are placed on the tissue boundary. Moreover, the most complex task in the resolution of the DOT inverse problem is assembling and inverting the sensitivity matrix. This matrix describes the change observed at each measurement site due to slight variations in the internal optical properties of a given point inside the medium. Since the number of unknowns, points inside the medium, are much higher than the number of measurements, the sensitivity matrix is non square [22]. Therefore, its inversion requires the use of unstable pseudo inversion methods [23,24]. It would be ideal to perform internal measurements at all points, which makes the number of unknowns and measurements equal. Such data acquisition scheme showed a drastic improvement in the quality of the reconstructed tomographic images as demonstrated by other modalities [25]. Practically, this configuration increases the number of measurements, which reduces the under-determination of the inverse problem and makes the inversion of the sensitivity matrix more stable.

Accordingly, we previously introduced a new high resolution diffuse optical imaging technique termed Photo-Magnetic Imaging (PMI) [26]. In fact, PMI uses an alternative concept compared to the conventional photon fluence detection at the boundary. It monitors the internal temperature variations induced by the optical absorption of the medium when illuminated with NIR light. Later, the optical absorption of the medium is obtained by minimizing the difference between the spatiotemporal simulated and measured temperature maps. First, the spatiotemporal distribution of temperature inside the medium is recorded using Magnetic Resonance Thermometry (MRT). Fundamentally, proton resonance frequency (PRF) decreases when hydrogen bonding decreases due to the temperature increase. By using one of the phase sensitive MRI sequences, a proportional relationship is established between the phase accumulation and temperature change between successive frames [27,28]. Afterwards, the simulated spatiotemporal temperature maps are generated by solving the combined diffusion and Pennes' bio-heat equations [2,29–31]. Based on the principle of optical absorption of the medium, this system of equations models the distribution of photons inside the medium and conversion of their energy to bio-heat [28,32]. Therefore, solving the forward problem of PMI consists in the resolution of this system of equations, generally performed using Finite Element Method (FEM).

Although our first generation PMI reconstruction algorithm can provide high resolution optical absorption images, two main aspects need to be improved. First, the FEM-based reconstruction algorithm cannot utilize the full measured data provided by the high resolution MRT images. The FEM procedure is initiated by mapping the measured MRT temperature maps on the FEM mesh nodes. During this step, the spatial resolution of the measurements is drastically degraded due to the fact that the number of nodes is much smaller than the number of pixels of MRT images. In fact, this degradation can be reduced using extra fine meshes. However, increasing the number of nodes makes the sensitivity matrix considerably larger and amplifies the complexity of the inverse problem that prolongs the overall reconstruction time.

The second weakness of the FEM-based algorithm is related to the resolution of the inverse problem, which starts by assembling the sensitivity matrix. In DOT, the number of unknowns is much higher than the number of measurements and the assembly of the

sensitivity matrix is generally performed using the adjoint-method to accelerate the process [2,22]. On the other hand, using MRT, the number of unknowns is equal to the number of measurements which makes the use of the adjoint-method inadequate as will be explained in the following sections. Therefore, the sensitivity matrix is computed using the perturbation method, by sequentially varying the absorption at each node and then solving the forward problem to determine the induced temperature change. This method is very time consuming and requires very heavy computational resources.

These two weaknesses can be overcome using analytic methods. Both diffusion [33–45] and Pennes' bio-heat equations [46–50] have been extensively solved analytically on regular geometries such as cylindrical, spherical and infinite or semi infinite slabs. These methods directly provide continuous spatiotemporal distribution of temperature inside the studied medium [51]. Using these analytic solutions not only accelerates the resolution of the forward problem but allow us to take advantage of the full high resolution data as well. Here, we present the framework of the second generation PMI reconstruction algorithm. In this new algorithm, the forward problem is solved analytically. This allows us to avoid MRT-to-mesh mapping of the high resolution MRT temperature measurements. Also, analytic solutions are not only fast but provide solutions as accurate as FEM. Unlike our first generation PMI algorithm, this new reconstruction algorithm is not iterative and provides the absorption map of the medium directly. Moreover, a new analytic technique is used to assemble the sensitivity matrix, which considerably reduces the computation time. The performance of our new analytic-based reconstruction algorithm is evaluated using both simulated and experimental data. Finally, the acceleration in the computation time is quantified by comparing reconstruction times of our first and second generation algorithms.

2. Methods

PMI uses a NIR light to heat the probed medium and monitor its internal temperature increase with MRT. A dedicated forward model generates the spatiotemporal temperature maps using the combined diffusion and Pennes' bio-heat equations system to model the photon migration and heat diffusion, respectively. These simulated temperature maps are later used during the resolution of the inverse problem.

2.1. Forward problem

The PMI image reconstruction algorithm requires the resolution of a combined diffusion and bio-heat equations system. PMI uses a continuous wave (CW) laser to warm up the medium. The CW light propagation in turbid media is generally modeled by the CW form diffusion equation [22,33]

$$-\nabla D\nabla\Phi(\boldsymbol{r})+\mu_a\Phi(\boldsymbol{r})=S(\boldsymbol{r})\,. \quad (1)$$

Here, Φ, $D(\mathbf{r})=\frac{1}{3[\mu_a(\mathbf{r})+\mu_s'(\mathbf{r})]}$, μ_a,μ_s' are the photon density, the diffusion coefficient, the absorption coefficient, and the reduced scattering coefficient, respectively. S is the isotropic

light source positioned $1/\mu_s'$ under the surface as imposed by diffusion approximation as shown in figure 1.

The temperature variation and propagation within the medium can be modeled by the Pennes' bio-heat equation. Although the photon density within the medium is steady, temperature is a function of time that requires the solution of the following time-dependent form

$$\rho c \frac{\partial T(\boldsymbol{r},t)}{\partial t} = \nabla[k \nabla T(\boldsymbol{r},t)] + E(\boldsymbol{r}). \quad (2)$$

Here, ρ, c and k represent the density, specific heat and thermal conductivity, respectively. The thermal energy absorbed from the laser heating is given by the product of the absorption distribution and the light fluence rate, $E(r) = \mu_a \Phi(r)$ [32]. It is important to note that the blood perfusion is omitted in this work but needs to be accounted for during *in-vivo* studies.

In our previous work [45], we obtained a comprehensive analytical solution for the diffusion equation based on an integral method for the Robin boundary condition. This solution is obtained by deriving a particular Green's function based on the integral method. Based on the assumption that the diffusion coefficient is spatially invariant, equation (1) becomes

$$-\nabla^2 \Phi(\boldsymbol{r}) + \frac{\mu_a}{D}\Phi(\boldsymbol{r}) = \frac{\gamma}{D}\delta(\boldsymbol{r},\boldsymbol{r}') \quad (3)$$

for a point light source modeled by the Dirac delta function $\delta(r, r')$ where r' and γ are the position and the strength of the light source, respectively.

The solution of the homogeneous diffusion equation in 2D cylindrical polar coordinates for a Dirac delta like point source was previously presented [45]. Implementing this photon density solution in equation (2), and using the separation of variables method lead to the final expression describing the laser induced temperature variations [51].

$$T(r,\theta,t) = T_s + \sum_{m=-\infty}^{\infty}\sum_{l=0}^{\infty} \frac{\rho c}{k\lambda_l^2}\omega_{m,l} J_m(\lambda_l r)\cos(m\theta)[1-\exp(\frac{-k}{\rho c}\lambda_l^2 t)]. \quad (4)$$

Here,

$$\omega_{m,l} = \frac{\mu_a}{\rho c}\{ - a_m(\beta) r_i [\beta J_{m-1}(\beta r_i) J_m(r_i \lambda_l) - \lambda_l J_m(\beta r_i) J_{m-1}(r_i \lambda_l)] \quad (5)$$

$$+ b_m(\beta) r_i [\beta J_{m-1}(\beta r_i) J_m(r_i \lambda_l) - \lambda_l J_m(\beta r_i) J_{m-1}(r_i \lambda_l)]$$

$$- \beta R J_{m-1}(R\beta) J_m(R\lambda_l) + R\lambda_l J_m(R\beta) J_{m-1}(R\lambda_l)$$

$$+ c_m(\beta) r_i [\beta Y_{m-1}(\beta r_i) J_m(r_i \lambda_l) - \lambda_l Y_m(\beta r_i) J_{m-1}(r_i \lambda_l)]$$

$$- \beta R Y_{m-1}(R\beta) J_m(R\lambda_l) + R\lambda_l Y_m(R\beta) J_{m-1}(R\lambda_l)\}$$

$$\times \frac{1}{\frac{1}{2} R(\beta^2 - \lambda_l^2)\left\{ R[J_{m-1}(R\lambda_l)^2 + J_m(R\lambda_l)^2] - \frac{2m J_{m-1}(R\lambda_l) J_m(R\lambda_l)}{\lambda_l} \right\}}$$

where

$$a_m(\beta) = \frac{\gamma \cos(m\theta_i)}{2D[2D\beta\xi R J_{m-1}(\beta R) + (R - 2Dm\xi) J_m(\beta R)]} \quad (6)$$

$$\times \{ J_m(\beta r_i)[2D\beta\xi R Y_{m-1}(\beta R) + (R - 2Dm\xi) Y_m(\beta R)]$$

$$+ Y_m(\beta r_i)[- 2D\beta\xi R J_{m-1}(\beta R) - (R - 2Dm\xi) J_m(\beta R)]\},$$

$$b_m(\beta) = \gamma R \frac{D\beta\xi[Y_{m-1}(\beta R) - Y_{m+1}(\beta R)] + Y_m(\beta R)}{2D[2D\beta\xi R J_{m-1}(\beta R) + (R - 2Dm\xi) J_m(\beta R)]} \times J_m(\beta r_i) \cos(m\theta_i), \quad (7)$$

$$c_m(\beta) = - \frac{\gamma}{2D} J_m(\beta r_i) \cos(m\theta_i) \quad (8)$$

where $\beta = i\sqrt{\frac{\mu_a}{D}}$, i is the complex number, R is the radius of the medium, ξ is a constant corresponding to the mismatch refractive index between the medium and its surrounding, J_m and Y_m are the Bessel functions of the first and second kind, respectively. During the derivation of this final solution, equation (4), the following heat convection boundary condition is used

$$-k\frac{\partial T(r)}{\partial t} = h(T_s - T(r)) \quad (9)$$

where h and T_s are the heat transfer coefficient and the surrounding temperature, respectively. During the derivation of this solution, we assumed that all optical and thermal properties are homogeneous. We also assumed that the spatial and temporal parts of the heat equation can be separable since we utilized the separation of variables method. Moreover, we approximated the light source by the Dirac delta function [51].

2.2. Inverse problem

High resolution absorption maps are obtained by solving the inverse problem of PMI. Technically, it consists in minimizing the quadratic difference between the measured MRT and the simulated temperature maps according to the following objective function

$$\Omega(\mu_a) = \sum_{p=1}^{N_p} \|T_p^M - F_p(\mu_a)\|^2 \quad (10)$$

where N_p represents the total number of pixels within the medium. T_p^M is the high resolution MRT temperature measured at pixel p. The forward operator F_p provides the simulated temperature at pixel $p = 1, 2, \ldots N_p$ using the spatial distribution of the absorption coefficient μ_a as expressed by equation (4). Equation (10) is minimized using the Levenberg-Marquard minimization [23,52]

$$\Delta\mu_a = (J^T J + \lambda I)^{-1} J^T (T_P^M - F_p(X_{init}(\mu_a)))^2 \quad (11)$$

with $\Delta\mu_a(N_p \times 1)$ being the update to the unknown vector of μ_a, obtained considering the initial distribution of absorption X_{init}. λ is the regularization parameter and I is the identity matrix. J is the sensitivity matrix also called Jacobian, describing the effect of an absorption variation at any point within the medium on the measured temperatures [2]

$$J_{\mu_a} = \frac{\partial T}{\partial \mu_a}. \quad (12)$$

2.3. Analytic sensitivity matrix

It is generally established that when performing DOT reconstructions using FEM, the sensitivity matrix is computed using the adjoint-method [22]. This method states that the influence of a source "s" on a detector "d" is the same as the influence of "d" on "s" when "d" is used as source and "s" as detector. Using this formulation, the Jacobian is simply obtained by solving the forward problem $N_S + N_D$ times, where N_S and N_D are the number

of sources and detectors, respectively. This adjoint-method significantly reduces the Jacobian assembly time and the overall computation time [7]. Using MRT to measure the internal spatiotemporal temperature of the medium is equivalent to placing a detector at each node of the FEM mesh. This configuration makes the use of the adjoint-method inadequate for the computation of the Jacobian since it loses its advantage due to high number of detectors. Therefore, the Jacobian is computed using the perturbation approach by varying the absorption at each node individually then solving the forward problem to establish a relationship between the absorption change at this node and the induced temperature variation at any point. Evidently, this straightforward method is very time consuming and requires very heavy computational resources.

Obtaining the Jacobian analytically requires the implementation of a new solution that can perform on a homogeneous medium with an absorbtion perturbation at a single point then deriving it. To our knowledge, such an analytical computation would be very complex and has not been done yet. Therefore, we introduce a new method to analytically assemble the Jacobian and implement it into our new analytic-based PMI reconstruction algorithm. Our analytic solution to the combined diffusion and bio-heat equation systems, is derived using a homogeneous absorption distribution within the medium. Hence, we first utilize the FEM-based algorithm to understand the dependence of the shape and amplitude of the Jacobian at any point as a function of optical and thermal properties of the medium. Please note that medium properties are varied over a wide range during these calculations. This empirical approach allows us to understand the relationship between these parameters and the shape as well as the amplitude of the Jacobian.

During this empirical approach, the first step is to compute the Jacobians for all the N FEM nodes (J_n, $n = 1, 2, ..N$), using our FEM-based solver while varying the optical and thermal properties of a synthetic phantom. Although we repeat these calculations over a wide range of optical and thermal properties, here we will present an example case with a certain set of parameters to explain this step in detail. Figure 2 shows a 40 mm diameter circular synthetic phantom whose absorption and reduced scattering coefficients are set to 0.01 mm^{-1} and 0.8 mm^{-1}, respectively. Meanwhile, the phantom is assumed thermally homogeneous where the density, specific heat and thermal conductivity are set to 1000 kg m^{-3} and 4200 J (kg C°)$^{-1}$, and 0.5 10^{-3} W (mm C°)$^{-1}$, respectively. The light is illuminated from the bottom of the phantom and the laser power is optimized in order to allow a maximum heating under 2 C° at the illumination site as shown in figure 2(a).

Figure 2(b) shows the temperature simulated after 8 seconds of heating with light using our FEM-based algorithm. This simulation uses a very fine mesh (Mesh_1) which consists of 65536 triangular elements connected at 33025 nodes. The Jacobian J_n at each node is computed using the perturbation method. After that, each individual Jacobian is mapped into a 200 pixel × 200 pixel grid to express them in cartesian coordinates. As an example, figure 2(c) shows the Jacobian J_n obtained at one of the nodes whose coordinates are $x_0 = 0$ mm and $y_0 = -15$ mm. Unlike the banana shape sensitivity matrix observed in diffuse optical tomography [22], the obtained Jacobian J_n consists in a kernel centered at this point as shown in figure 2(c).

The Jacobian for each set of optical and thermal properties is first calculated for all nodes and then mapped into the Cartesian grid. Afterwards, extensive series of fitting are performed to investigate all the aforementioned parameters. Based on these fittings, we establish that the distribution of the Jacobian J_n at any node $n(x_0, y_0)$ can be expressed as

$$J_n(x, y) = A_n(x_0, y_0)J_s(x - x_0, y - y_0) \quad (13)$$

where $A_n(x_0,y_0)$ is the amplitude of the kernel and J_s is the shape of the kernel, which is obtained by normalizing the kernel fitted on the Jacobian computed on that node $n(x_0, y_0)$. This shows that the amplitude and the normalized shape of each Jacobian can be independently studied. Accordingly, we investigate them separately as a function of the parameters of the medium and the spatial position within the phantom.

2.3.1. Shape of the Kernel (J_s)—To investigate the shape of the kernels, a series of fittings is performed on all the Jacobians computed with FEM at each node $n(x_0, y_0)$. Figure 3(a) shows an example of the fitted kernel on the Jacobian J_n obtained at a particular node (x = 0 mm, y = −15 mm) as shown in figure 2(c). After normalizing the fitted kernels, we observe that the shape of the kernel is found to be governed only by the optical and thermal properties of the phantom and is totally independent from the strength of the laser source and the spatial position within the medium. In other words, the normalized shape of the kernel is found to be the same for a given set of optical and thermal properties. The normalized shape of the kernel, $J_s = \tilde{J}_n/max(\tilde{J}_n)$, is given by

$$J_s(x, y) = \exp\left[\left(-3.12\mu_a^{0.58} - 2.41\right)\left(\frac{\kappa}{\rho c}\right)^{0.27}\sqrt{(x - x_0)^2 + (y - y_0)^2}\right]. \quad (14)$$

The profiles performed on both Jacobians J_n and $\tilde{J}_n$ are in very good agreement as shown in figure 3(b). Please note that these fittings are verified not only for each node in a particular synthetic phantom but also for a large range of optical and thermal properties. Although the fitting is performed on Jacobians computed at the nodes, it is important to mention that equation (14) is valid for any point within the medium and allows us to calculate J_s at any point (x, y) in the cartesian grid.

2.3.2. Amplitude of the Kernel (A_n)—Unlike the shape of the kernel, J_s, its amplitude, A_n, exhibits a strong dependence on the spatial position within the medium in addition to the dependence on the optical and thermal properties. Implementing an analytical formula to obtain the amplitude of the kernel, A_n, with respect to its spatial position and background optical properties is complicated. In this paper, we propose an alternative method that allows us to obtain A_n in two steps.

Since analytic solutions can be obtained only on homogeneous media, first the so called *Total Jacobian*, J_T, is computed using equation (12) by varying the absorption coefficient of all pixels simultaneously instead of varying it locally at a given pixel. Since this step is performed using analytic methods, cartesian coordinates are used and all the positions are

defined as pixels that belong to the 200 × 200 grid. Accordingly, the *Total Jacobian*, J_T, corresponds to the sum of all the individual Jacobians J_n centered at each pixel $n(x_0, y_0)$ and can be written as:

$$J_T(x,y) = \sum_{x=0}^{N_x} \sum_{y=0}^{N_y} J_n(x,y) \quad (15)$$

where N_x and N_y are the size of the grid describing the domain, containing the phantom, in the x– and y– directions, respectively. By substituting equation (13) into equation (15), we obtain

$$J_T(x,y) = \sum_{x=0}^{N_x} \sum_{y=0}^{N_y} A_n(x_0,y_0) J_s(x-x_0, y-y_0). \quad (16)$$

Equation (16) shows that by definition, J_T at any pixel is then given by the convolution of the normalized kernel $J_s(x, y)$ and the amplitude of the kernel $A_n(x_0, y_0)$ at pixel $n(x_0, y_0)$ so that we can write

$$J_T = A_n \otimes J_s. \quad (17)$$

From equation (17), $A_n(x, y)$, the amplitude of the kernels at any position within the phantom is simply obtained by deconvolving the normalized kernel J_s from the Total Jacobian, J_T,

$$A_n = J_T \otimes^{-1} J_s. \quad (18)$$

Figures 4(a)–4(c) show the *Total Jacobian* (J_T) map, the normalized analytic kernel (J_s), and the maximum amplitudes (A_n) of the individual Jacobians obtained using our new algorithm. Since both J_s and J_T are noise free, the deconvolution can be performed using any deconvolution method without any difficulty. In the following calculations, the deconvolution is performed using the Lucy-Richardson deconvolution algorithm [53]. Once the maximum amplitudes A_n are obtained analytically, the analytic Jacobians are assembled using equation (13).

To validate our approach, we compare the computed maximum amplitudes using equation (18) with the amplitude of the FEM-based individual Jacobians chosen at random points. Figure 4(d) shows that the profile of A_n, along the white dashed-line, matches perfectly the amplitudes obtained with the FEM-based algorithm at nodes (x = 0 mm, y = −17.5, −15, −12.5 mm). In summary, our new analytic Jacobian assembly method is performed following these steps. First, the distribution of the Jacobian J_s is obtained using equation (14). Secondly, the *Total Jacobian* J_T is obtained using equation (12) by varying the

absorption coefficient of the whole medium instead of a local variation at one given position. Afterwards, the amplitude of the Jacobian at each pixel A_n is obtained by simply deconvolving J_s from J_T. Following that, the Jacobian J at any point $n(x_0, y_0)$ is obtained using equation (13), multiplying the shape function by its corresponding amplitude at that particular point $n(x_0, y_0)$. Finally, the obtained Jacobian J is used in the PMI inverse problem as expressed by equation (11).

2.4. Simulation studies

The performance of our new PMI reconstruction algorithm is first tested with simulation studies. Using our FEM-based forward solver, synthetic measurements are generated by first calculating the photon density distribution in the medium using equation (1) then simulating the photon thermal energy deposition and the temperature propagation at any point and any time using equation (2). The numerical phantom used in this study mimics the phantom used in the validation of the forward problem of our FEM-based solver [54]. The same 40 mm diameter cylindrical synthetic phantom described in section 2.3 is utilized for this study. In order to model an optical heterogeneity, however, two 5 mm diameter cylindrical inclusions are embedded 4.5 mm below the illuminated surface of the phantom (edge-to-center) and positioned 8.5 mm apart as shown in Figure 5. The absorption of both inclusions is set to be four times higher than the background ($\mu_a = 0.04\ mm^{-1}$) while no scattering contrast is introduced. Figure 5 shows a cross- section of the cylindrical phantom and the laser beam used to heat it up. The laser power and the irradiated area are matched to those used in the previous experimental studies [54].

2.5. Experimental studies

A dedicated small animal PMI system has been developed in our laboratory as shown in figures 6(a) and 6(b). A customized animal interface, with four ports for illumination purpose, is placed in the center of a Philips 3 Tesla Achieva MR scanner. An 808 nm, high power fiber coupled laser (Focuslight, China) is used to illuminate the imaged phantom. Although our system is equipped with 4 laser ports, only the port at the bottom of the phantom is used in this experiment. The high power laser is placed on a copper heat sink with TEC thermoelectric cooler using temperature feedback control. The laser, its driver, TEC cooling unit and computer that generates signals for MRI synchronization are all positioned in the control room due to the high magnetic fringe field. Light is transported from the laser to the surface of the phantom via 15-meter long optical fiber. A 35 mm diameter Newport aspherical lens is placed at the end of the fiber to collimate the output laser in order to provide uniform illumination over a spot diameter of 13.5 mm. The laser power level is set to 1.2 W resulting in a power density of 840 mW/cm^2 at the surface.

The laser-induced temperature is measured by MRT using the proton resonance frequency shift method. A temperature map is acquired every 8 seconds using a gradient echo sequence with a repetition time (TR) and echo time (TE) set to 80 ms and 48 ms, respectively. Figure 6(c) shows the timeline for MRT acquisition. First, a T1 weighted sequence is performed to precisely locate the laser position in the axial direction. Following that, a dynamic imaging set consisting of multiple frames (8 seconds each) is started. The first image of the dynamic MRT set is acquired prior turning the laser on and used as the baseline phase map (frame 1).

Once it is completed, the laser is then turned on and the second frame is acquired. Post processing is performed afterwards to calculate the laser induced temperature variation based on the phase shift between the second frame and baseline [54]. This high resolution temperature map is used as measured data in the PMI image reconstruction algorithm, equation (11).

3. Results

3.1. Simulation results

In order to validate our new method, absorption maps are obtained using our new analytic-based reconstruction algorithm and compared with those obtained with our FEM-based reconstruction algorithm. For both FEM- and analytic-based algorithms, the synthetic temperature map is generated using our FEM-based PMI forward solver as shown in figure 7(b). This temperature map clearly shows the laser induced temperature increase under the illumination site. Also, this map already reveals the position of both inclusions prior to any reconstruction process. In fact, due to their higher absorption, the temperature rises more within the inclusions [55]. However, the low spatial resolution of the temperature map, mainly due to heat diffusion, does not allow a precise localization of the inclusions. In order to overcome the effect of diffusion and obtain quantitative absorption maps, the PMI inverse problem needs to be solved.

First, in order to optimize the computation time of our FEM-based reconstruction algorithm, a coarser mesh (Mesh_2) is used rather than Mesh_1, which is utilized to generate the synthetic temperature map. Mesh_2 consists of 8192 triangular elements connected at 4225 nodes. Figures 7(c) and 7(d) show the reconstructed high resolution absorption maps obtained by our FEM-based reconstruction algorithm at the first and the second iterations, respectively. Actually, the algorithm is stopped automatically when the stop criteria -no more than 1% improvement- is met at the end of the second iteration. Figure 7(c) shows that the FEM-based algorithm is able to recover 71% of the true absorption value at the first iteration and a second iteration is needed to recover an additional 22% of the true absorption value as shown in figure 7(d). This can be clearly seen on the profiles carried-out along the dashed line passing by the center of the two inclusions as shown in figure 7(f). However, it is important to note that this iterative step is very time consuming. In fact, performing an additional iteration approximately doubles the overall computation time.

Figure 7(e) shows the reconstructed high resolution absorption map obtained using our new analytic method. This map shows that in addition to being non iterative, our new method provides comparable results to those obtained at the end of the FEM-based reconstruction algorithm. Quantitatively, the FEM-based algorithm recovers an absorption coefficient of $0.0365 \pm 0.0063\ mm^{-1}$ and our new method recovers a similar absorption of $0.0365 \pm 0.0064\ mm^{-1}$. However, our new results are much better than the results obtained at the first iteration of the FEM-based algorithm which only recovered an absorption value of $0.0287 \pm 0.0049\ mm^{-1}$ as can be seen of the profiles presented in figure 7(f).

Although the meshes used by the FEM-based method for reconstruction and data generation are different, using the same method in both steps gives the FEM-based reconstruction

algorithm an additional advantage. Despite this unfair advantage allowed for the FEM-based algorithm, our new method still seems more suitable considering the quality of its reconstructed images and its fast computation time. In fact, it is very important to emphasize that our new method is non iterative and requires only 2.8% of the computation time of one single iteration of the FEM-based reconstruction algorithm. In fact, only 51 seconds are necessary to provide an absorption map from a 200 pixel × 200 pixel MRT temperature map.

3.2. Experimental results

Figure 8(b) shows the 200 pixel × 200 pixel MRT temperature map measured on the agarose phantom used in the validation of the forward problem of our FEM-based solver [53]. The geometry of the phantom contains N_p = 31401 pixels of the MRT image. Similar to the simulated temperature map, the localization of both inclusions is possible on the MRT image prior to any reconstruction process. This is due to the higher increase in their temperature compared to the background of the phantom [55]. However, the temperature increase inside the inclusions is strongly dependent on the distance from the laser source, which necessitates the resolution of the PMI inverse problem. In the following, our new algorithm is experimentally validated by comparing the analytically reconstructed absorption maps with those obtained using our FEM-based algorithm. The FEM-based reconstructions are performed using Mesh_2. In order to initialize the measurements for the FEM-based algorithm, the 31401 measured MRT temperature map pixels are mapped to Mesh_2 which results in 86% loss of data. The reconstructed absorption maps obtained by our FEM-based algorithm with one and two iterations are presented in figures 8(c) and 8(d), respectively. On the other hand, our new analytic method is a pixel based reconstruction algorithm. Using a pixel size of 0.2 mm, the geometry of the numerical phantom fits inside a 200 pixel × 200 pixel grid, indicated by black dashed line in figure 8(a), of those 31401 pixels are within the circular geometry (gray area as shown in figure 7(a)). All these 31401 measured MRT temperature map pixels are directly used to initialize the measurements for the analytic-based method, and no mapping nor interpolation is needed yielding to no data loss. Despite the noise present in the measured MRT map, the inclusions are recovered successfully on all three reconstructed absorption maps and their locations are in very good agreement with the cross-section of the phantom presented in figure 8(a). However, the FEM-based algorithm is not able to correctly recover the circular shape of the inclusions as shown in figures 8(c) and 8(d). Moreover, the absorption map obtained at the first iteration recovered only 58.25% of the real absorption and a second iteration is needed to recover an additional 12.75%, Table 1.

Figure 8(e) shows that our new method is more robust to noise due to the higher amount of data used in the resolution of the inverse problem. In fact, in addition to being very fast, our new method recovers the circular shape of the inclusions more successfully with high quantification accuracy, Table 1. It is however important to note the slight artifact observed at the boundary under the illumination site. Actually, the laser is collimated and has a beam diameter of 13.5 mm at the surface of the phantom while our analytic-based method models the laser as a point source. This difference in the source beam size is responsible for these slight artifacts under the illuminated surface. Nevertheless, these slight artifacts do not degrade the quantification accuracy of our method as you can see on the profiles presented in figure 8(f). These profiles show that our new method provides better results than those

obtained at the end of the FEM-based algorithm. In addition, our new analytic-based results are obtained approximately 30 times faster than one single iteration of the FEM-based algorithm.

4. Conclusion

We have previously introduced PMI, a new multi-modality technique that provides high resolution optical absorption maps. By combining MRI and optical imaging, PMI leverages the high spatial resolution of MRI and the high sensitivity of optical imaging. The main innovation of PMI is the interaction between optical and MRI modalities to break optical scattering barrier and produce higher resolution optical absorption images. The superior performance of our FEM-based PMI was demonstrated with both simulation and experimental studies earlier [26,55]. The bottleneck of the FEM-based image reconstruction algorithm is mainly the assembly of the Jacobian matrix during the iterative resolution of the inverse problem. In fact, the Jacobian is assembled using the perturbation method that consists in solving the forward problem for each node after varying its absorption. Thus, our FEM-based PMI reconstruction process requires heavy computational resources and long computation time.

In this paper, we present a new fast and non iterative analytical based reconstruction method for PMI. First, our new algorithm uses an analytic method to solve the forward problem and gain considerable computation time by avoiding any mesh generation or system matrix assembly, which are necessary and time-consuming processes in FEM. However, this analytical method can perform only in homogeneous media. This limits our new reconstruction algorithm to a single iteration which is equivalent to linearizing the nonlinear PMI inverse problem. Nevertheless, our analytic method has the advantage of avoiding the inefficient mapping of the high resolution MRT temperature measurements to the FEM mesh. This allows the direct use of the whole MRT measurements and eliminates the data loss in the mapping step. In addition, the major advantage of this new algorithm consists in the fast analytical implementation of the Jacobian matrix which drastically reduces the computation time. In fact, an acceleration of 30-fold is obtained which yields a high resolution absorption image (200 pixel × 200 pixel) in 51 seconds. This reconstruction time can be reduced even farther by either increasing the pixel size, i.e. by reducing the resolution, or by parallelizing the codes on a graphic processing unit.

The PMI optical absorption maps can be used for diagnostic purposes. In fact, intrinsic tissue contrast can be used to identify cancerous tissue based on its higher absorption contrast. Alternatively, highly absorbing contrast agents such as gold nanoparticles can be utilized to differentiate diseased tissue for diagnostic purposes. Moreover, PMI can play a key role in providing therapy guidance. For instance, these high resolution optical absorption maps can be utilized to optimize the laser pulse duration and the mean power density for laser thermal therapy. Our future work would focus on the implementation of new Jacobian-free optimization method and the adaptation of this algorithm for multi-wavelength, and in-vivo PMI applications.

Acknowledgments

This research is supported in part by Fulbright awarded to Dr. Nouizi, NIH grants, F31CA171915-01A1, SBIRHHSN261201300068C, 1R21CA191389, R21EB013387, R01EB008716, P30CA062203, TUBITAK Grant 2219, Bogazici University Research funding Grant No. BAP 7126 and TUBITAK Grant No. 112T253.

References

1. Hebden J, Arridge S, Delpy D. Optical imaging in medicine. I. Experimental techniques. Phys. Med. Biol. 1997; 42:825. [PubMed: 9172262]
2. Arridge SR, Hebden JC. Optical imaging in medicine: II. Modelling and reconstruction. Phys. Med. Biol. 1997; 42:841. [PubMed: 9172263]
3. Gibson A, Hebden J, Arridge SR. Recent advances in diffuse optical imaging. Phys. Med. Biol. 2005; 50:R1. [PubMed: 15773619]
4. Gibson A, Dehghani H. Diffuse optical imaging. Philos. Trans. A Math. Phys. Eng. Sci. 2009; 367:3055. [PubMed: 19581255]
5. Dehghani H, Srinivasan S, Pogue BW, Gibson A. Numerical modelling and image reconstruction in diffuse optical tomography Philos Trans A. Math. Phys. Eng. Sci. 2009; 367:3073.
6. Koenig A, Hervé L, Da Silva A, Dinten JM, Boutet J, Berger M, Texier I, Peltié P, Rizo P, Josserand V, Coll J. Whole body small animal examination with a diffuse optical tomography instrument. Nucl. Instrum Meth. A: Accelerators, Spectrometers, Detectors and Associated Equipment. 2007; 571:56.
7. Nouizi F, Torregrossa M, Chabrier R, Poulet P. Improvement of absorption and scattering discrimination by selection of sensitive points on temporal profile in diffuse optical tomography. Opt. Express. 2011b; 19:12843–12854. [PubMed: 21716527]
8. Lapointe E, Pichette J, Brub-Lauzire Y. A multi-view time-domain non-contact diffuse optical tomography scanner with dual wavelength detection for intrinsic and fluorescence small animal imaging. Rev. Sci Instrum. 2012; 83:063703. [PubMed: 22755630]
9. Unlu MB, Birgul O, Shafiiha R, Gulsen G, Nalcioglu O. Diffuse optical tomographic reconstruction using multifrequency data. J. Biomed. Opt. 2006; 11:054008. [PubMed: 17092157]
10. EganWG, , HilgemanTW. New York: Academic; 1979Optical Properties of Inhomogeneous Materials.
11. QuartoG, , TorricelliA, , SpinelliL, , PifferiA, , CubedduR, , TaroniP. Advanced Time-Correlated Single Photon Counting ApplicationsSpringer; 2015587611
12. Jiang S, Pogue BW, Kaufman PA, Gui J, Jermyn M, Frazee TE, Poplack SP, DiFlorio-Alexander R, Wells WA, Paulsen KD. Predicting breast tumor response to neoadjuvant chemotherapy with diffuse optical spectroscopic tomography prior to treatment. Clin. Cancer Res. 2014; 20:6006. [PubMed: 25294916]
13. Tromberg BJ, Pogue BW, Paulsen KD, Yodh AG, Boas DA, Cerussi AE. Assessing the future of diffuse optical imaging technologies for breast cancer management. Med. Phys. 2008; 35:2443. [PubMed: 18649477]
14. Eggebrecht AT, Ferradal SL, Robichaux-Viehoever A, Hassanpour MS, Dehghani H, Snyder AZ, Hershey T, Culver JP. Mapping distributed brain function and networks with diffuse optical tomography. Nat. Photonics. 2014; 8:448. [PubMed: 25083161]
15. NouiziF, , Diaz-AyilG, , BléF-X, , DuboisB, , UhringW, , PouletP. Timegated near-infrared spectroscopic imaging of brain activation: a simulation proof of concept. In: SPIE, editorSPIE BIOSSan Francisco: International Society for Optics and Photonics; 2011a78960L–L–8
16. Singh H, Cooper RJ, Wai Lee C, Dempsey L, Edwards A, Brigadoi S, Airantzis D, Everdell N, Michell A, Holder D, Hebden JC, Austin T. Mapping cortical haemodynamics during neonatal seizures using diffuse optical tomography: a case study. Neuroimage Clin. 2014; 5:256. [PubMed: 25161892]
17. Montcel B, Chabrier R, Poulet P. Time-resolved absorption and hemoglobin concentration difference maps: a method to retrieve depth-related information on cerebral hemodynamics. Opt. Express. 2006; 14:12271. [PubMed: 19529655]

18. Nouizi F, Torregrossa M, Geneveaux O, Chabrier R, Poulet P. 3D modeling of noncontact fiber-based approach for time-resolved diffuse optical tomography. SPIE BiOS: International Society for Optics and Photonics. 2011c:78961Z–Z–8.
19. MuY, , NiedreM. A fast SPAD-based small animal imager for early-photon diffuse optical tomography; Engineering in Medicine and Biology Society (EMBC), 2014 36th Annual International Conference of the IEEE: IEEE); 201428332836
20. Lin Y, Thayer D, Nalcioglu O, Gulsen G. Tumor characterization in small animals using magnetic resonance-guided dynamic contrast enhanced diffuse optical tomography. J. Biomed. Opt. 2011; 16:106015. [PubMed: 22029362]
21. Arridge SR, Lionheart WRB. Non-uniqueness in diffusion-based optical tomography. Opt. Lett. 1998; 23:882. [PubMed: 18087373]
22. Arridge S. Optical tomography in medical imaging. Inverse Problems. 1999a; 15:R41.
23. Marquardt DW. An algorithm for least squares estimation of nonlinearpaameters. J. Soc. Ind. Appl. Math. 1963a:431.
24. Yalavarthy PK, Pogue BW, Dehghani H, Paulsen KD. Weight-matrix structured regularization provides optimal generalized least-squares estimate in diffuse optical tomography. Med. Phys. 2007; 34:2085. [PubMed: 17654912]
25. Woo EJ, Seo JK. Magnetic resonance electrical impedance tomography (MREIT) for high-resolution conductivity imaging. Physiol. Meas. 2008; 29:R1. [PubMed: 18799834]
26. Lin Y, Gao H, Thayer D, Luk AL, Gulsen G. Photo-magnetic imaging: resolving optical contrast at MRI resolution. Phys. Med. Biol. 2013; 58:3551. [PubMed: 23640084]
27. Kickhefel A, Roland J, Weiss C, Schick F. Accuracy of real-time MR temperature mapping in the brain: a comparison of fast sequences. Phys. Med. 2010; 26:192. [PubMed: 20096617]
28. Rieke V, Butts Pauly K. MR thermometry. J. Magn. Reson. Imaging. 2008; 27:376. [PubMed: 18219673]
29. Arridge S. Photon-measurement density functions. Part I: Analytical forms. Appl. Opt. 1999b; 34:7395.
30. Schweiger M, Arridge SR, Hiraoka M, Delpy DT. The finite element method for the propagation of light in scattering media: boundary and source conditions. Med. Phys. 1995; 22:1779. [PubMed: 8587533]
31. Wissler EH. Pennes' 1948 paper revisited. J. Appl. Physiol. 1985; 85:35.
32. Diaz SH, Aguilar G, Lavernia EJ, Wong BJF. Modeling the thermal response of porcine cartilage to laser irradiation. IEEE. J. Sel. Topics Quantum Electron. 2001; 7(6):944.
33. Arridge SR, Cope M, Delpy DT. The theoretical basis for the determination of optical pathlengths in tissue: temporal and frequency analysis. Phys. Med. Biol. 1992; 37:1531. [PubMed: 1631197]
34. Boas DA, O'Leary MA, Chance B, Yodh AG. Scattering of diffuse photon density waves by spherical inhomogeneities within turbid media: analytic solution and applications. Proc. Natl. Acad. Sci. USA. 1994; 91:4887. [PubMed: 8197151]
35. Walker SA, Boas DA, Gratton E. Photon density waves scattered from cylindrical inhomogeneities: theory and experiments. Appl. Opt. 1998; 37:1935. [PubMed: 18273113]
36. Pogue BW, Patterson MS. Frequency-domain optical absorption spectroscopy of finite tissue volumes using diffusion theory. Phys. Med. Biol. 1994; 39:1157. [PubMed: 15552104]
37. Contini D, Martelli F, Zaccanti G. Photon migration through a turbid slab described by a model based on diffusion approximation. I. Theory. Appl. Opt. 1997; 36:4587. [PubMed: 18259254]
38. Kienle A, Patterson MS. Improved solutions of the steady-state and the time-resolved diffusion equations for reflectance from a semi-infinite turbid medium. J. Opt. Soc. Am. A Opt. Image Sci. Vis. 1997; 14:246. [PubMed: 8988618]
39. Kienle A. Light diffusion through a turbid parallelepiped J. Opt. Soc. Am. A Opt. Image Sci. Vis. 2005; 22:1883.
40. Martelli F, Sassaroli A, Del Bianco S, Zaccanti G. Solution of the time-dependent diffusion equation for a three-layer medium: application to study photon migration through a simplified adult head model. Phys. Med. Biol. 2007; 52:2827. [PubMed: 17473354]

41. Liemert A, Kienle A. Light diffusion in a turbid cylinder. I. Homogeneous case. Opt. Express. 2010a; 18:9456. [PubMed: 20588792]
42. Cong W, Wang LV, Wang G. Formulation of photon diffusion from spherical bioluminescent sources in an infinite homogeneous medium. Biomed. Eng. Online. 2004; 3:12. [PubMed: 15125780]
43. Sikora J, Zacharopoulos A, Douiri A, Schweiger M, Horesh L, Arridge SR, Ripoll J. Diffuse photon propagation in multilayered geometries. Phys. Med. Biol. 2006; 51:497. [PubMed: 16424578]
44. Liemert A, Kienle A. Light diffusion in N-layered turbid media: frequency and time domains. J. Biomed. Opt. 2010b; 15:025002. [PubMed: 20459243]
45. Erkol H, Nouizi F, Unlu MB, Gulsen G. An extended analytical approach for diffuse optical imaging. Phys. Med. Biol. 2015b; 60:5103. [PubMed: 26083326]
46. Brix G, Seebass M, Hellwig G, Griebel J. Estimation of heat transfer and temperature rise in partial-body regions during MR procedures: an analytical approach with respect to safety considerations. J. Magn. Reson. Im. 2002; 20:65.
47. Jaunich M, Raje S, Kim K, Mitra K, Guo Z. Bio-heat transfer analysis during short pulse laser irradiation of tissues. Int. J. Heat Mass Tran. 2008; 51:5511.
48. Deng ZS, Liu J. Mathematical modeling of temperature mapping over skin surface and its implementation in thermal disease diagnostics. Comput. Biol. Med. 2004; 34:495. [PubMed: 15265721]
49. Jiang L, Zhan W, Loew MH. Modeling static and dynamic thermography of the human breast under elastic deformation. Phys. Med. Biol. 2011; 56:187. [PubMed: 21149948]
50. Neufeld E, Chavannes N, Samaras T, Kuster N. Novel conformal technique to reduce staircasing artifacts at material boundaries for FDTD modeling of the bioheat equation. Phys. Med. Biol. 2007; 52:4371. [PubMed: 17634638]
51. Erkol H, Nouizi F, Luk A, Unlu MB, Gulsen G. Comprehensive analytical model for CW laser induced heat in turbid media. Opt. Express. 2015a; 23:31069. [PubMed: 26698736]
52. Levenberg K. A method for the solution of certain non-linear problems in least squares. Q. Appl. Math. 1944; 2:164.
53. Richardson WH. Bayesian-Based Iterative Method of Image Restoration. JOSA. 1972; 62(1):55.
54. Thayer DA, Lin Y, Luk A, Gulsen G. Laser-induced photo-thermal magnetic imaging. Appl. Phys. Lett. 2012; 101:83703. [PubMed: 22991481]
55. Nouizi F, Luk A, Thayer D, Lin Y, Ha S, Gulsen G. Experimental validation of a high-resolution diffuse optical imaging modality: photomagnetic imaging. J. Biomed. Opt. 2016; 21(1):16009. [PubMed: 26790644]

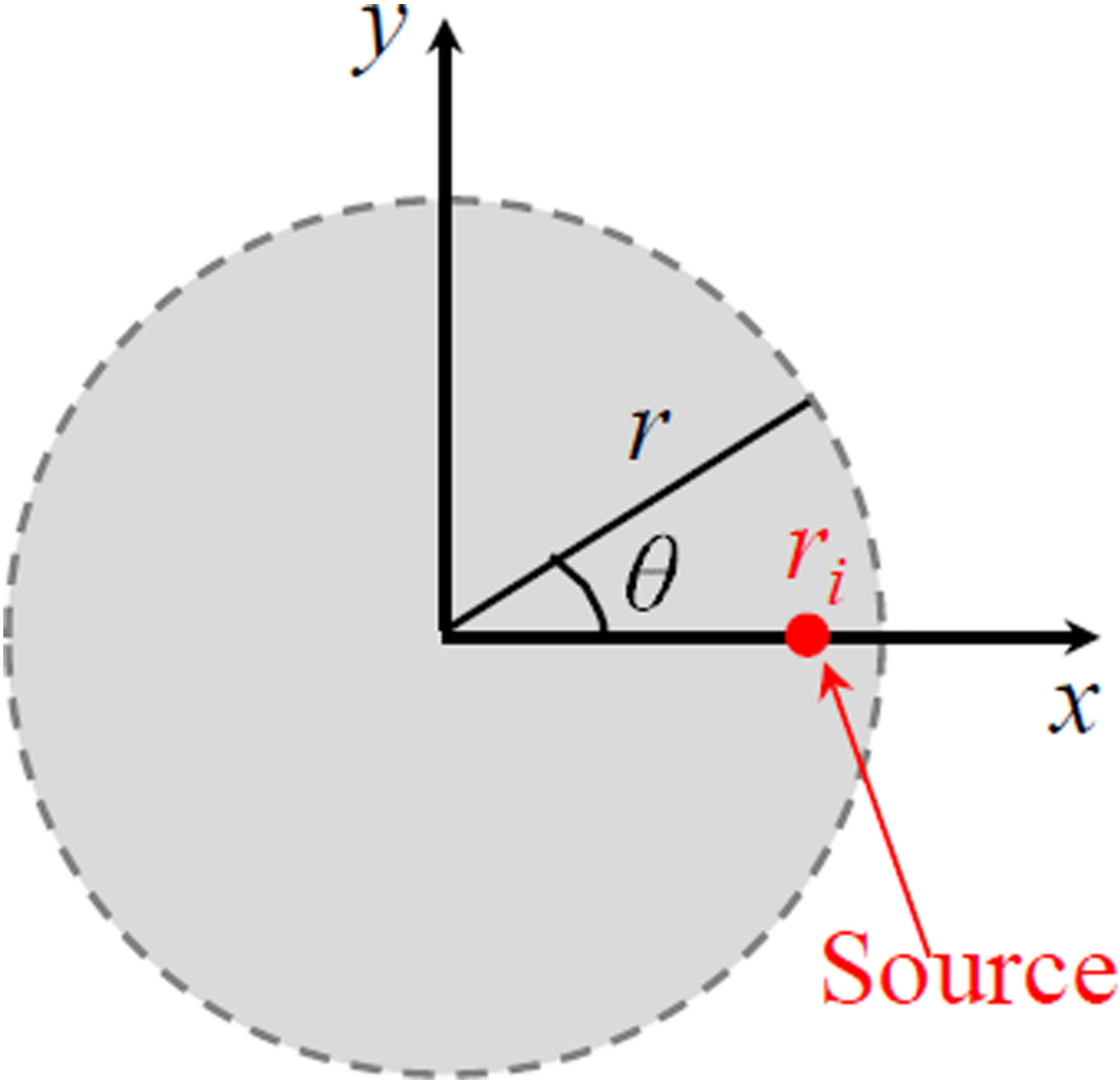

Figure 1.
Schematic of the geometry of a homogeneous medium with a delta function source in 2D.

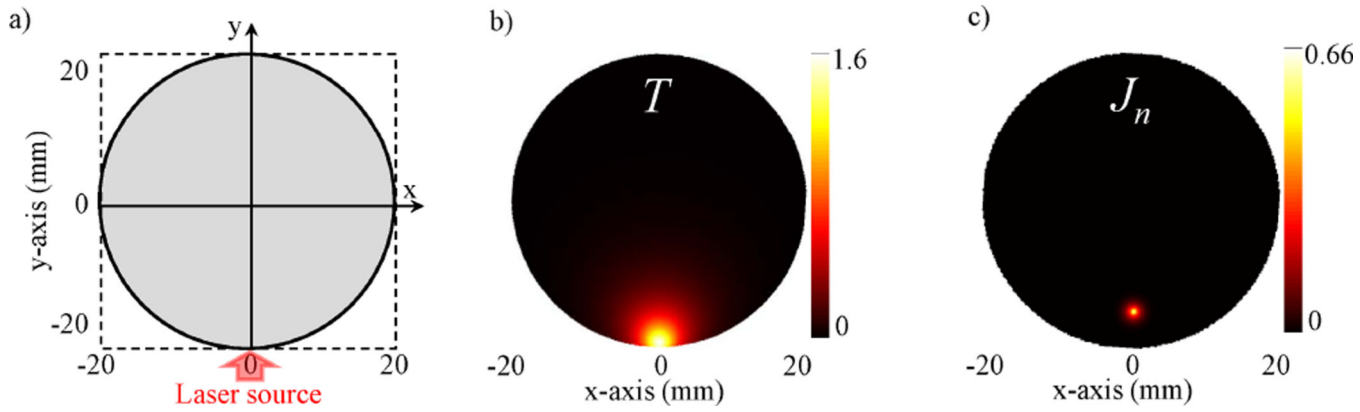

Figure 2.

a) Schematic showing the synthetic phantom and the position of the laser source. b) The simulated temperature obtained by solving the FEM-based PMI forward problem, 8 seconds after turning on the laser. c) The Jacobian computed with the FEM-based algorithm at a particular node ($x = 0$ mm, $y = -15$ mm).

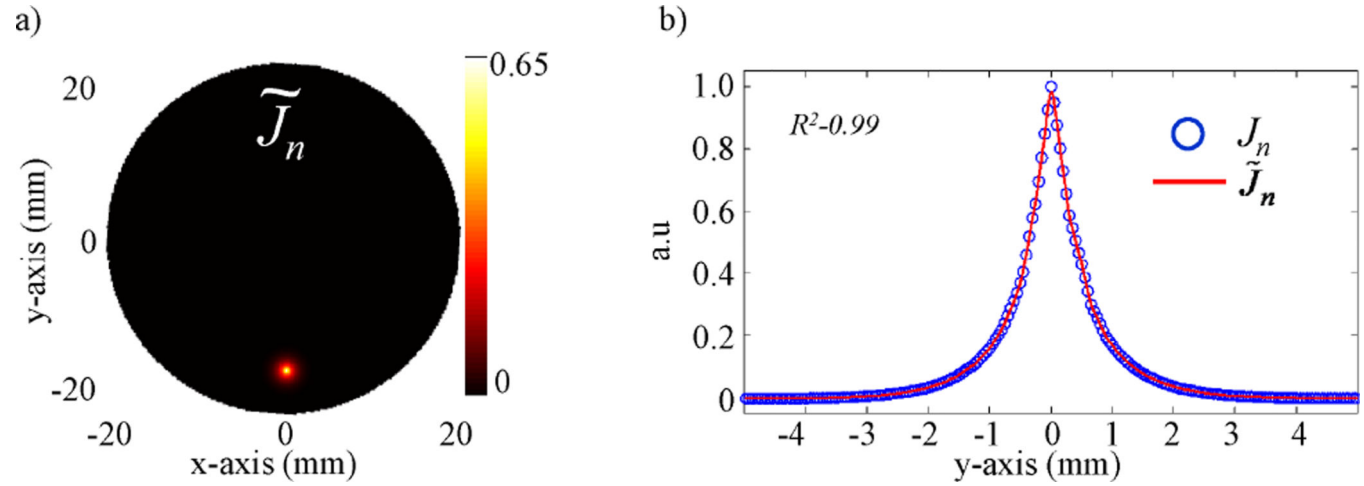

Figure 3.

The analytic Jacobian $\tilde{J}_n$ fitted on $\tilde{J}$, the Jacobian obtained using our FEM-based solver at a particular node ($x = 0$ mm, $y = -15$ mm). b) The normalized profiles performed on $\tilde{J}_n$ and $\tilde{J}$.

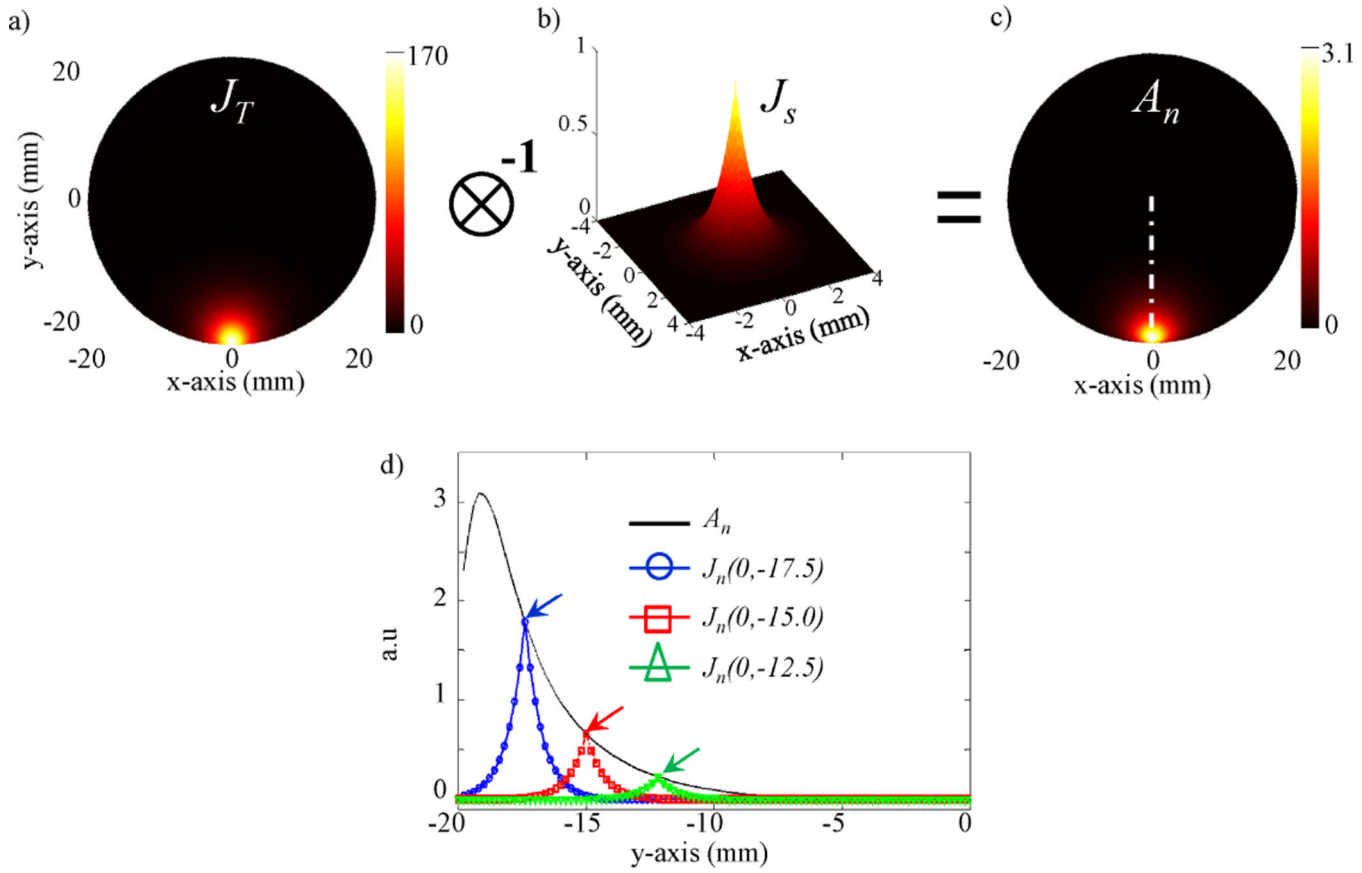

Figure 4.

a) *The Total Jacobian*, J_T, obtained by changing the absorption simultaneously at all nodes. b) The normalized shape of the kernel obtained using equation (15). c) A_n of the individual Jacobians obtained using our new algorithm. e) The profile carried-out on A_n, along the white dashed-line, matches the maximum amplitude of the individual Jacobians computed using the FEM-based algorithm at nodes ($x = 0$ mm, $y = -17.5,-15,-12.5$ mm). The arrows show that the amplitudes of the kernels computed using both the analytic-based and the FEM-based algorithms are in perfect agreement.

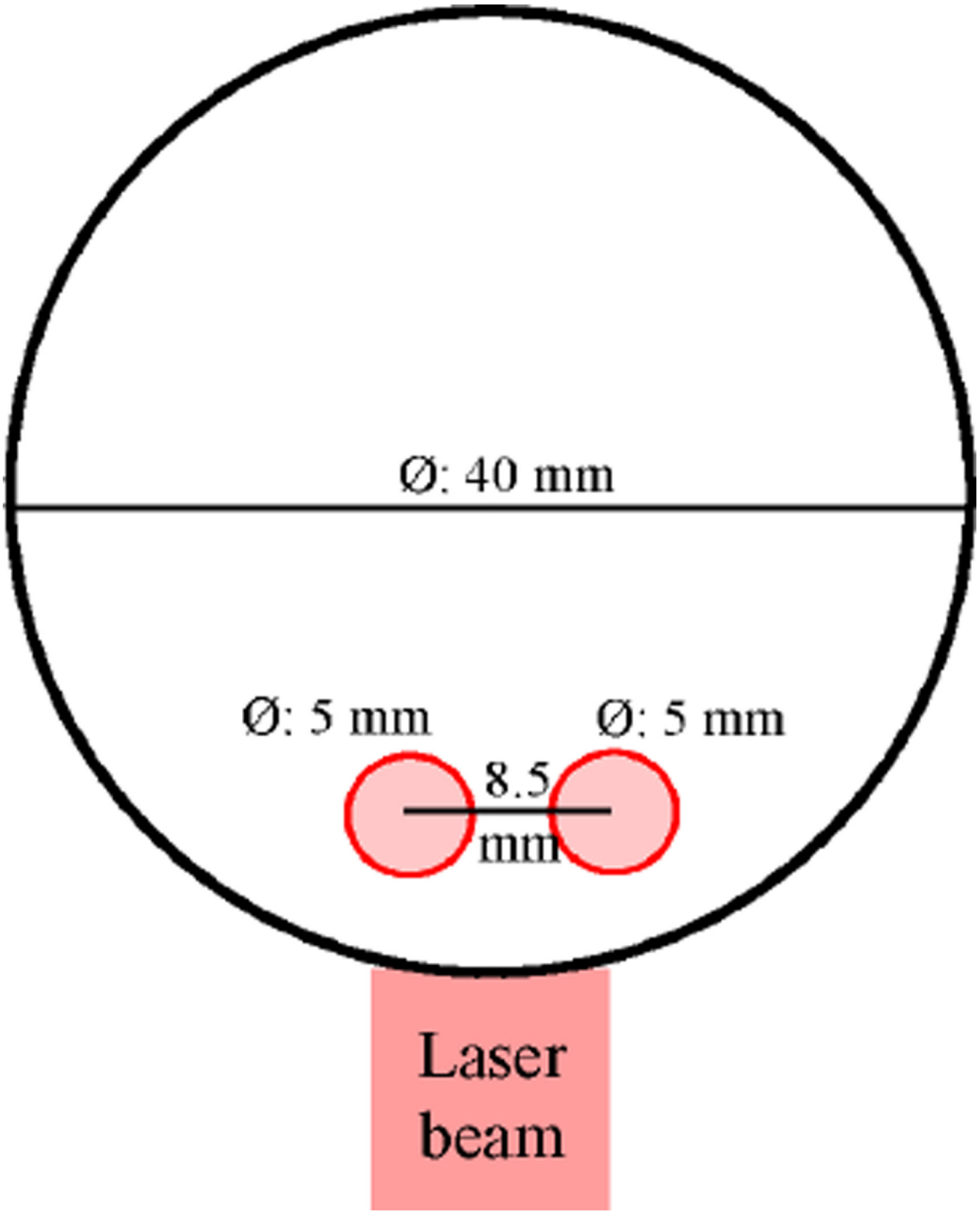

Figure 5.
Schematic of the 40 mm diameter cylindrical phantom containing two 5 mm diameter inclusions placed 8.5 mm apart and 4.5 mm below the illuminated surface. The absorption of both inclusions is set to be four times higher than the background, while no scattering contrast is introduced.

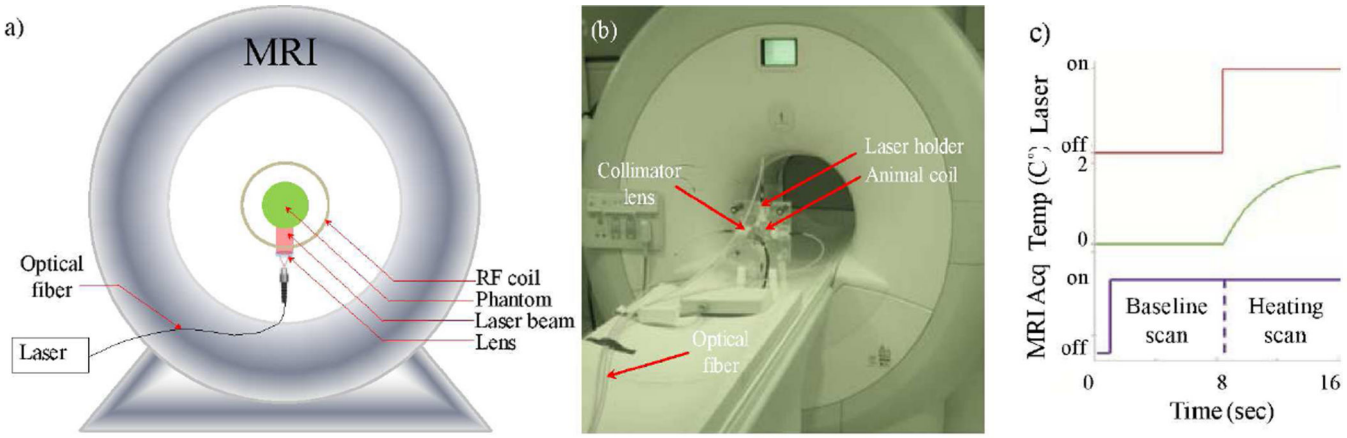

Figure 6.

a) Schematic of the PMI setup showing the optical instrumentation, the RF coil for MRI acquisition and the phantom inside the MRI bore. b) Picture of the PMI interface placed on the bed of a Philips 3 Tesla Achieva system. There are four ports for laser illumination with collimator lenses. c) The schematic of PMI data acquisition timeline.

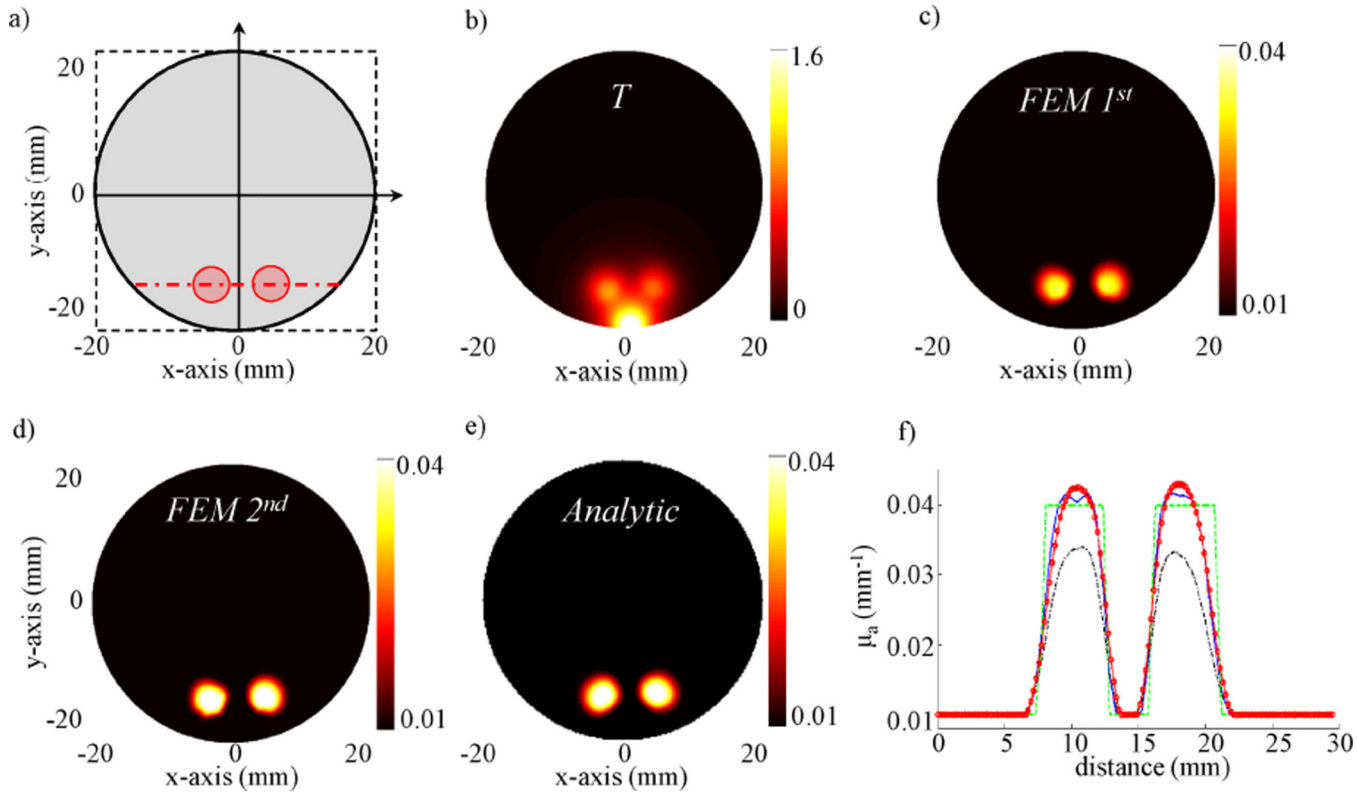

Figure 7.

a) Schematic of the double inclusion numerical phantom. The two times more absorbent inclusions are shown with red circles while the limits of the pixel grid is shown in a black dashed line. b) The synthetic temperature map simulated at the end of the heating cycle (8 seconds after turning on the laser). c) The reconstructed absorption map using one iteration of the FEM-based algorithm. d) The final reconstructed absorption map using the FEM-based algorithm. e) The reconstructed absorption map using our analytic-based algorithm. f) The reconstructed absorption profiles along the centers of the two inclusions: real (dashed green line), reconstructed using the new analytical method (red line with circle marker), reconstructed using one iteration of the FEM-based algorithm (dash-dot black line) and reconstructed at the final iteration of the FEM-based algorithm (blue line).

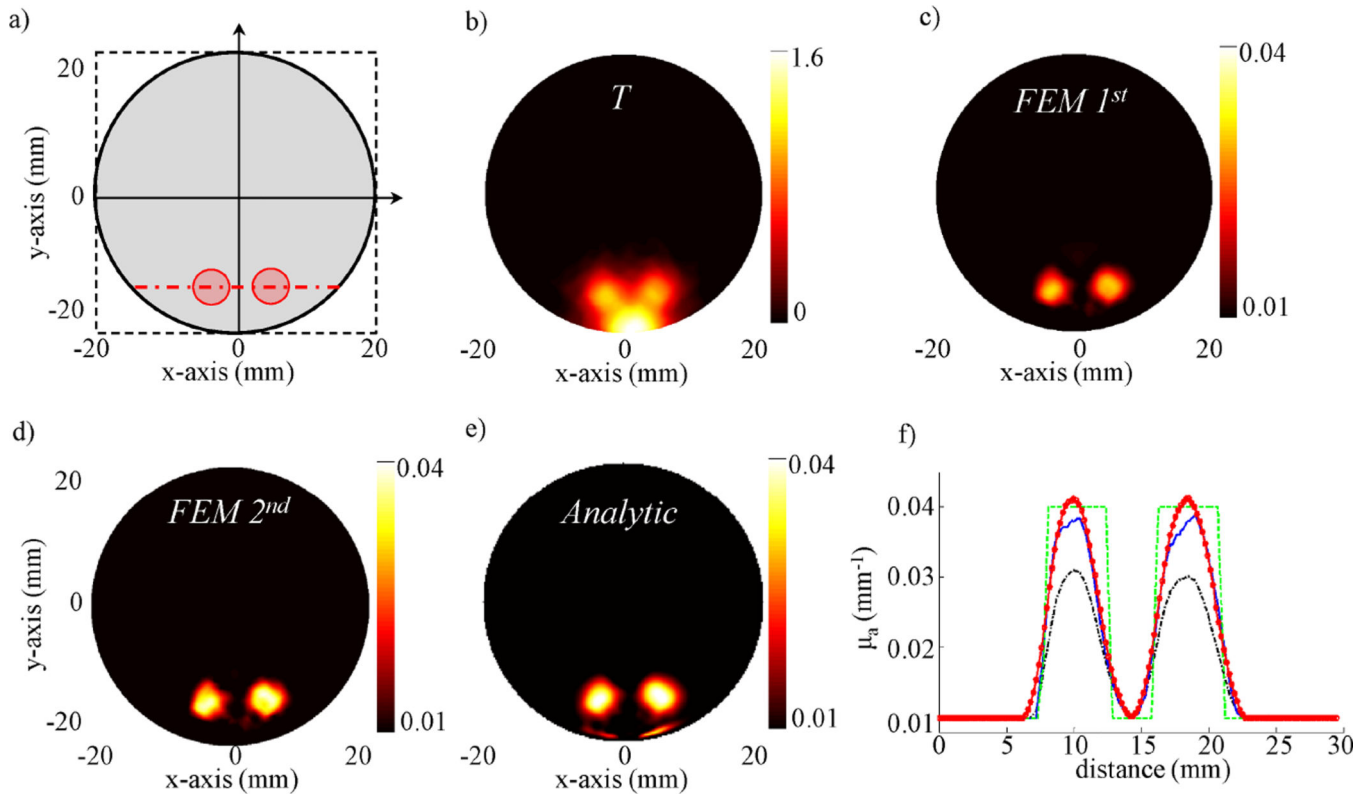

Figure 8.

a) Schematic of the double inclusion agar phantom. The two times more absorbent inclusions are shown with red circles while the limits of the pixel grid is shown in a black dashed line. b) The high resolution MRT temperature map measured at the end of the heating cycle (8 seconds after turning on the laser). c) The reconstructed absorption map using one iteration of the FEM-based algorithm. d) The final reconstructed absorption map using the FEM-based algorithm. e) The reconstructed absorption map using our analytic-based algorithm. f) The reconstructed absorption profiles along the centers of the two inclusions: real (dashed green line), reconstructed using the new analytical method (red line with circle marker), reconstructed using one iteration of the FEM based algorithm (dash-dot black line) and reconstructed at the final iteration of the FEM based algorithm (blue line).

Table 1

Summary of PMI experimental results performed with the double inclusion phantom. The mean value and the standard deviation of the reconstructed optical absorption are reported for both inclusions and the background.

	Left inclusion		Right inclusion		Background	
	$\mu_a(mm^{-1})$	Error (%)	$\mu_a(mm^{-1})$	Error (%)	$\mu_a(mm^{-1})$	Error (%)
Real	0.04	/	0.04	/	0.01	/
FEM 1st	0.0233 ± 0.0045	41.2	0.0246 ± 0.0039	38.1	0.0101 ± 0.0004	1.0
FEM 2nd	0.0284 ± 0.0061	28.8	0.0310 ± 0.0052	21.8	0.0101 ± 0.0004	1.0
Analytic	0.0309 ± 0.0069	22.3	0.0333 ± 0.0065	16.0	0.0102 ± 0.0013	2.0